



OPEN ACCESS

EDITED BY

Stefano Leone,
Fraunhofer IAF, Germany

REVIEWED BY

Georg Schönweger,
University of Kiel, Germany
Yunfei He,
University of Pennsylvania, United States

*CORRESPONDENCE

Kapil Saha,
✉ saha.k@northeastern.edu

RECEIVED 27 January 2025

ACCEPTED 04 March 2025

PUBLISHED 02 April 2025

CITATION

Saha K, Simeoni P, Colombo L and Rinaldi M (2025) Piezoelectric and ferroelectric measurements on casted target-deposited $Al_{0.45}Sc_{0.45}B_{0.1}N$ thin films. *Front. Mater.* 12:1567614. doi: 10.3389/fmats.2025.1567614

COPYRIGHT

© 2025 Saha, Simeoni, Colombo and Rinaldi. This is an open-access article distributed under the terms of the [Creative Commons Attribution License \(CC BY\)](https://creativecommons.org/licenses/by/4.0/). The use, distribution or reproduction in other forums is permitted, provided the original author(s) and the copyright owner(s) are credited and that the original publication in this journal is cited, in accordance with accepted academic practice. No use, distribution or reproduction is permitted which does not comply with these terms.

Piezoelectric and ferroelectric measurements on casted target-deposited $Al_{0.45}Sc_{0.45}B_{0.1}N$ thin films

Kapil Saha*, Pietro Simeoni, Luca Colombo and Matteo Rinaldi

ECE Department, NanoSI Institute, Northeastern University, Boston, MA, United States

This study reports on the characterization of a 45% scandium-doped Aluminum Nitride (AlScN) thin films co-doped with 10% Boron (B). AlScBN thin films were deposited on Si (100) 200 mm wafers using a pulsed DC reactive magnetron sputtering system. A 4" casted alloy target of $Al_{0.45}Sc_{0.45}B_{0.1}N$ was used in the depositions. The influence of deposition parameters, including target-substrate distance, N_2 flow rate, and deposition temperature, on the films' crystallinity and surface characteristics was investigated on silicon substrates. The crystalline properties of the thin films were characterized using X-ray diffraction (XRD) method with 2θ and ω scans. Based on the characterization performed on Si, process conditions were selected to deliver the best crystallinity while maintaining a stable plasma. Parameters were set to a target-substrate distance of 65 mm, a flow rate of 30 sccm, and a deposition temperature of 300°C. Under these process conditions, a 564 nm-thick sample was fabricated for piezoelectric and ferroelectric characterization. Several capacitive structures of different areas were prepared using a tungsten (W) blanket bottom electrode and platinum (Pt) top electrode on a double-side polished Si substrate. The $d_{33,f}$ coefficient was measured through Piezoelectric Measurement (PZM) technique using Double Beam Laser Interferometry (DBLI) system, yielding a value of ~ 25 pm/V. Ferroelectric characteristics were assessed through Dynamic Hysteresis Measurement (DHM) and Positive-Up, Negative-Down (PUND) measurement techniques using the same tool. The film exhibited a coercive field $E_c^+ = 1.5$ MV/cm, $E_c^- = 2.5$ MV/cm and a remnant polarization ($2P_r$) of 280 μCcm^{-2} .

KEYWORDS

piezoelectricity, ferroelectricity, MEMS, thin films, sputtering, AlScBN

1 Introduction

Piezoelectric and ferroelectric materials are critical for microacoustic devices in applications such as sensing (Muralt et al., 2009; Fawzy and Zhang, 2019), acoustic communication (Xue et al., 2024), and RF filtering (Muralt, 2008; Azarnaminy et al., 2024). Among the piezoelectric materials, Aluminum Nitride (AlN) is particularly of interest due to its high acoustic velocity (Tabrizian et al., 2009), high thermal conductivity (Tabrizian et al., 2009), and compatibility with complementary metal-oxide semiconductor (CMOS)

processes (Haider et al., 2023). Nevertheless, the low piezoelectric coefficients of AlN have restricted its performance in applications that require high electromechanical coupling (Manna et al., 2018).

To overcome this trade-off, there have been significant research thrusts to increase the piezoelectric coupling of AlN by introducing additional elements in the crystal, with the notable success of scandium (Sc) doping, which significantly enhances both the piezoelectric and ferroelectric properties of the material and is currently being deployed for commercial applications (Wingqvist et al., 2010; Matloub et al., 2013; Olsson et al., 2020; Startt et al., 2023). This enhancement was first reported by researchers who demonstrated considerable improvements in the piezoelectric response of Sc-doped AlN thin films prepared by dual reactive co-sputtering (Akiyama et al., 2010; Kurz et al., 2019; Beaucejour et al., 2022). Ab-initio models and experimental results reported in literature (Tasnádi et al., 2010; Caro et al., 2015; Akiyama et al., 2009) indicate that Sc concentrations up to 43% can substantially enhance the piezoelectric response (d_{33}) of AlN films and reported a four-fold increase, yielding a value of 27.6 pC/N. Additionally, a d_{33} value of 31.6 pC/N has been reported recently for 41% Sc-doped AlN (Lu et al., 2018b), while Kenji, Hirata et al. demonstrated that the incorporation of a lutetium (Lu) buffer layer could stabilize the wurtzite phase of ScAlN beyond the 43% Sc doping limit, resulting in a d_{33} value of 35.5 pC/N for 50.8% ScAlN (Hirata et al., 2025). However, neither of these values was obtained using Double Beam Laser Interferometry (DBLI) method, which has been identified as more accurate than the Berlincourt method (Piezometer), as reported by Zhaorong, Huang et al. (Huang et al., 2006). Furthermore, in these d_{33} measurements conducted using the Piezometer, the influence of electrode size relative to substrate thickness was not considered, which could lead to measurement inaccuracies (Sivaramakrishnan et al., 2013). In this study, the DBLI method has been employed for d_{33} calculation to ensure greater precision, which is a vital keypoint for this experimental study. Moreover, AlScN has exhibited ferroelectric properties (Fichtner et al., 2019), unlocking potential applications in ferroelectric memory devices and related technologies (Gund et al., 2021; Liu Z. et al., 2023). Another doping element that has drawn attention for its potential impact on AlN properties is Boron (B). Substituting B in AlN has demonstrated notable enhancements in ferroelectric responses (Zhu et al., 2021; Liu Z. et al., 2023), making AlBN a suitable option for advanced memory applications (Hayden et al., 2021).

Expanding upon this research, Jing et al. (Jing et al., 2022) performed a theoretical investigation utilizing density functional theory (DFT) simulations to explore the co-doping effect of Sc and B in AlN. Their findings indicated that the incorporation of a specific concentration of boron (B) into AlScN not only improves the piezoelectric stress coefficient (e_{33}) and elastic constant (C_{33}) but also provides new perspectives on surpassing the previously proposed Sc doping threshold of 43% (Akiyama et al., 2009). Analysis of crystal structure and bonding revealed that boron doping decreases the lattice parameter ratio (c/a), resulting in an elevated average strain coefficient (d_{33}). This study aims to investigate experimentally the properties of $Al_{0.45}Sc_{0.45}B_{0.10}N$ thin films. With this goal in mind, the characterization of films deposited using a 4", 45% Al, 45% Sc, and 10% B casted target is reported. The crystallinity of the films is characterized via X-Ray diffraction (XRD)

and SEM visual inspection. The piezoelectric (d_{33}) and ferroelectric (P_r and E_c) responses of the AlScBN film were measured via double beam laser interferometry (DBLI), yielding $d_{33} = \sim 25$ pm/V, $2P_r = 280$ μ C/cm², and $E_c^+ = 1.5$ MV/cm, $E_c^- = 2.5$ MV/cm, respectively.

2 Experimental methods

AlScBN thin films were deposited on 200 mm Silicon (Si) (100) substrates using an Evatec® Clusterline-200 II magnetron sputtering system under high vacuum conditions, maintaining pressures around 10^{-8} mbar. A 4-inch casted target composed of $Al_{45}Sc_{45}B_{10}$ alloy was employed for the deposition process. Several parameters, including temperature, pressure, gas flow rate, and chuck height, were varied to influence the deposition conditions and the resulting film properties. The target was powered with a pulsed DC output of 900 W, operating at a pulse frequency of 150 kHz and an 88% cycle on time. To identify the optimal deposition conditions for AlScBN, the distance between the target and substrate was methodically varied while all other parameters were kept constant. These experiments allowed us to determine the deposition rate at each chuck height while maintaining a constant nitrogen (N_2) gas flow of 30 sccm. To calculate the deposition rate, a Woollam ESM-300 Ellipsometer was used. The Ellipsometer determines the thickness of thin films by analyzing the dependence of the polarization response on film thickness and refractive indices (Saha, 2023). Argon (Ar) gas was excluded from the depositions based on findings by Beaucejour et al. (Beaucejour et al., 2022), who reported that Argon can increase the number of abnormally oriented grains (AOGs) on the film surface. To detect the AOGs on the surface of the deposited films, a Zeiss Supra 25 Field Emission Scanning Electron Microscope (FE-SEM) was used. To minimize AOG formation, pure nitrogen was used with flow rates ranging from 20 to 30 standard cubic centimeters per minute (sccm). During the N_2 sweep, both chuck height and temperature were held constant to monitor changes in stress levels and crystallinity. Stress measurements of the thin films were conducted using a KLA-Tencor FLX-2320. The stress was quantified by measuring the curvature of the substrates before and after deposition, as determined using Stoney's equation (Stoney, 1909). X-ray diffraction (XRD) analysis was performed on AlScBN thin films deposited on Si (100) substrates to evaluate crystallinity using a PANalytical X'Pert Pro XRD tool. This instrument is equipped with a Philips PW3040/60 X-ray generator and contains a detector. To get diffraction data, the surface of the samples was exposed to $Cu - K\alpha$ X-ray radiation with a wavelength (λ) of 1.5418 Å. 2θ scans were performed to know the crystallographic planes present in the film, whereas rocking curve values from the ω scan curve implied the crystallinity. The relationship between c -axis alignment and piezoelectric properties in ScAlN thin films, as established by Tholander et al. (Tholander et al., 2015), was used as a basis for determining optimal deposition conditions. Additionally, a temperature sweep was conducted to assess the impact of deposition temperature on film quality, with tests performed at 300°C, 350°C, and 400°C. The results indicated that film crystallinity was highest at 300°C for a 200 mm substrate. A summary of the deposition parameters for AlScBN thin films on Si substrates, aimed at identifying an ideal recipe and understanding the influence of deposition factors on film quality, is provided in Table 1. Based

TABLE 1 Deposition parameters used for the sputtering process of AlScBN thin films.

Sample number	Substrate	T(°C)	N ₂ flow (sccm)	Chuck height (mm)	Power (W)	Time (sec)	Thickness (nm)	Stress (Mpa)
Sample 1	Si	300	30	33	900	2,250	305	-209
Sample 2	Si	300	30	50	900	2,250	263	-470
Sample 3	Si	300	30	65	900	2,808	302	-913
Sample 4	Si	300	25	65	900	2,645	299	-1,079
Sample 5	Si	300	20	65	900	2,500	300	-1,290
Sample 6	Si	350	30	65	900	2,800	304	-623
Sample 7	Si	400	30	65	900	2,800	301	-700
Sample S5	W	300	30	65	900	5,000	564	—

on the characterization data presented in this table, the optimal procedure for preparing AlScBN samples for piezoelectric and ferroelectric property investigations was identified.

A tungsten (W) layer was used as the bottom electrode on a 200 mm silicon (100) double-sided polished (DSP) substrate. Subsequently, a 564 nm-thick AlScBN thin film was deposited over the metal layer. To know the surface topology of this sample, roughness measurement was conducted utilizing a Park XE-7 Atomic Force Microscope (AFM) in non-contact mode. To facilitate the measurement of piezoelectric and ferroelectric responses, a 150 nm platinum (Pt) layer was deposited and patterned as the top electrode on the AlScBN film. The parallel-plate capacitors were patterned in circles and square shapes with different areas. Electrical access to the blanket bottom electrode was created by deliberately removing small portions of the piezoelectric surface through scratching. Indium (In) paste was applied to the scratched area to ensure proper electrical grounding of the bottom electrode. The piezoelectric properties of AlScBN were investigated utilizing an aixACCT Double-Beam Laser Interferometer (DBLI). The d_{33} measurement via DBLI combines laser interferometry on both the bottom and top sides of the substrate to quantify the voltage-dependent surface displacement of capacitors while accounting for substrate bending (Sivaramakrishnan et al., 2018; Liu C. et al., 2023). The ferroelectric properties of AlScBN were also studied using the same AixACCT system. Figures 1A, B illustrate the cross-sectional schematic of the DBLI sample (film stack: W-AlScBN-Pt) and the patterned top electrodes, respectively.

3 Results and discussion

3.1 Stress optimization

For the stress optimization, AlScBN films deposited on Si (100) 200 mm substrates were examined. The stress data and thickness of the deposited films, obtained from the Ellipsometer measurements, are summarized in Table 1. According to the data

reported in Table 1, it is notable that increasing the distance between the target and substrate can make the film more compressive. It is also evident that at constant temperature and target-substrate distance, the stress tends to be more compressive with decreasing order of N₂ gas flow.

Figure 2 illustrates the film's stress dependence on multiple process parameters, such as chuck height, N₂ flow rate, and temperature, as listed in Table 1. Figure 2A illustrates that the stress becomes more compressive as the chuck height increases. At reduced chuck heights, the stress is comparatively modest (-200 MPa); however, when the chuck height approaches to 65 mm, the stress drops to roughly -900 MPa. In contrast, the dependence of stress level on the N₂ flow rate exhibits an inverse relationship, as shown in 2(B). As the N₂ flow increases, the stress becomes less compressive. Increasing the N₂ flow rate from 20 sccm to 30 sccm changes the film stress from roughly -1,300 MPa to -900 MPa. Temperature significantly impacts stress levels. Stress demonstrates somewhat intricate behavior as temperature fluctuates, as indicated in 2(C). At a reduced temperature of 300°C, the stress is highly compressive (-1,290 MPa). Raising the temperature to 350°C reduces the film stress to -623 MPa. However, increasing the temperature to 400°C results in a more compressive film stress of -700 MPa compared to 300°C. Though we found the lowest stress at 350°C, for optimal process conditions, other process factors must also be considered.

3.2 Crystallographic orientation and crystallinity

The Gonio scan (2θ scan) was used to identify the crystallographic phases present in the film (Deng et al., 2024). Figure 3A illustrates the presence of different crystalline phases in the deposited AlScBN film, whereas Figures 3B–D show the variation of the peak angle of the AlScBN wurtzite phase (0002 phase) with the process parameters. As shown in Figure 3B, the peak position shifts to the left as the distance between the target

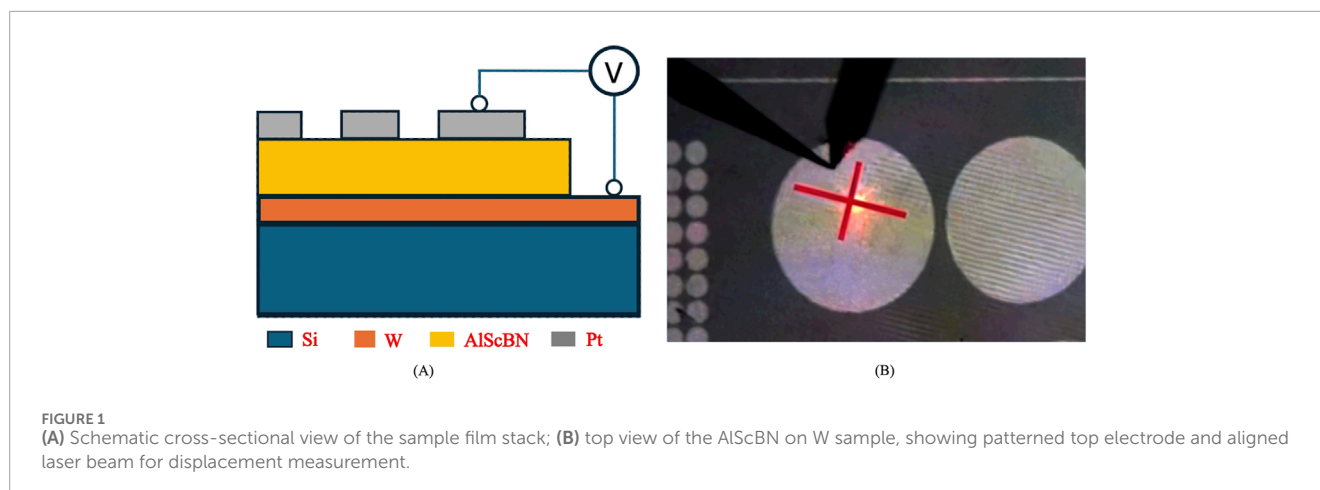


FIGURE 1 (A) Schematic cross-sectional view of the sample film stack; (B) top view of the AlScBN on W sample, showing patterned top electrode and aligned laser beam for displacement measurement.

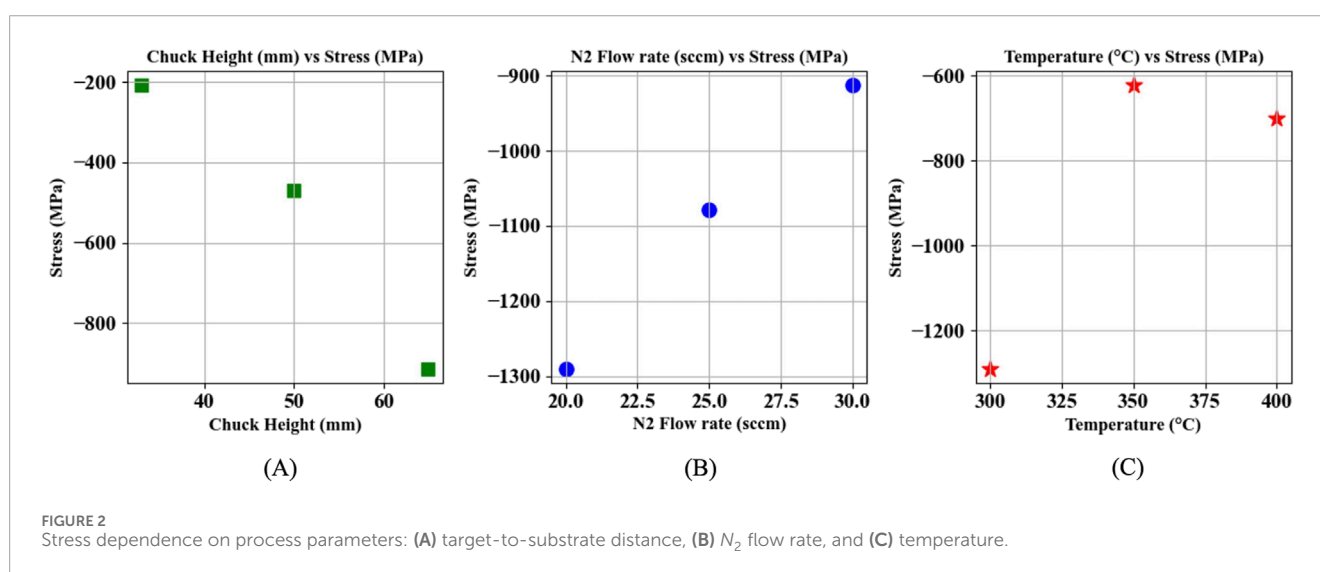


FIGURE 2 Stress dependence on process parameters: (A) target-to-substrate distance, (B) N_2 flow rate, and (C) temperature.

and substrate increases. Based on the information shown in Figures 3C, D, it can be observed that with a decrease in both the N_2 flow rate and temperature, the AlScBN 0002 peak shifts to the left. This is likely due to the effect of lower process pressure on the film residual stress (Pirro et al. (2022)). As shown in Figure 2B, the film's stress shifts towards more compressive values as the nitrogen flow is reduced.

The crystallinity of the deposited films was analyzed using the full width at half maximum (FWHM) of the ω scan (rocking curve) under various conditions, as shown in Figure 4. Figure 4A illustrates the ω scan data, highlighting the effect of the distance between the target and substrate on the crystallinity of the thin film. Optimal crystallinity was achieved at a distance of 65 mm with an FWHM of 2.16° . Shorter distances resulted in broader peaks, indicating inferior crystallinity. Figure 4B shows the influence of the nitrogen flow rate on film quality. The best crystallinity was observed at a nitrogen flow rate of 20 sccm, producing an FWHM of 1.98° . Higher flow rates of 25 sccm and 30 sccm resulted in slightly broader peaks, which indicates the impact of N_2 flow rate on the film crystallinity is not too influential. Figure 4C depicts the dependence of crystallinity on deposition temperature. The ideal temperature for deposition was

found to be 300°C , with an FWHM of 2.16° . Higher temperatures of 350°C and 400°C led to broader peaks, indicating a decline in crystallinity. These findings suggest that the best process conditions for depositing AlScBN thin films with superior crystallinity in this system are a target-substrate distance of 65 mm, a nitrogen flow rate of 20 sccm, and a deposition temperature of 300°C for 200 mm substrate. However, at a nitrogen flow rate of 20 sccm, the plasma was found to be unstable throughout the process because of the low pressure ($< 10^{-4}$ mbar), resulting in arcing during deposition. To stabilize the plasma by increasing the pressure and to strike a trade-off between stress and crystallinity, an N_2 flow rate of 30 sccm and a chuck height of 65 mm at 300°C were selected as the processing conditions for depositing the film on tungsten (W) substrate to evaluate the ferroelectric and piezoelectric responses of AlScBN. The crystallographic orientation of the sample deposited on W is illustrated in Figure 5. The wurtzite crystallographic phase (0002) exhibits a peak at 36.94° shown in Figure 5A, validating the outcome of the chosen process conditions. Figure 5B shows that the full width at half maximum (FWHM) of the omega curve is 3.49° , suggesting that further optimization on W substrates is possible compared to the films deposited on Si substrates.

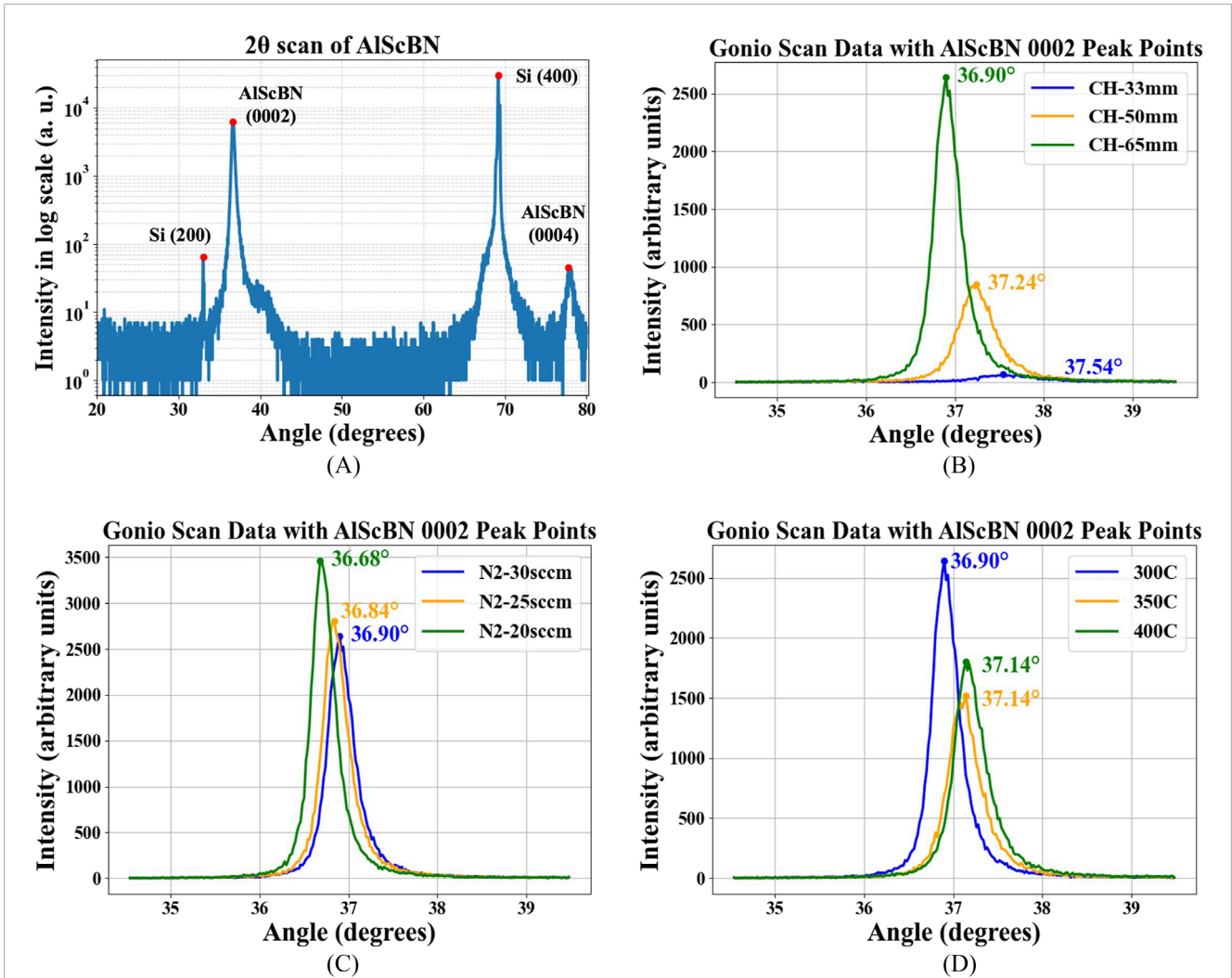


FIGURE 3 (A) XRD 2θ scan showing the crystalline phases present in the deposited AlScBN thin film. (B–D) Goniometer scans of the (0002) peak, highlighting its shift with varying (B) target-to-substrate distance, (C) N₂ flow rate, and (D) deposition temperature.

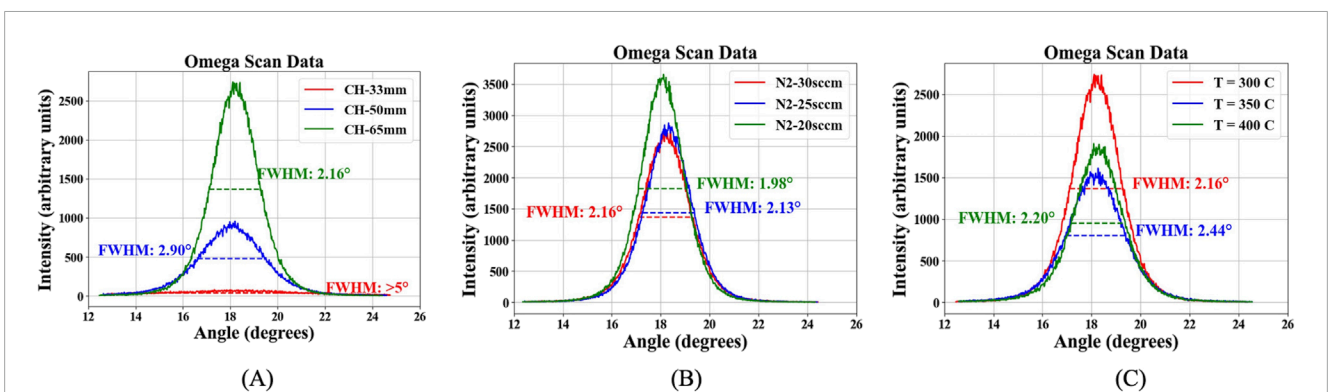
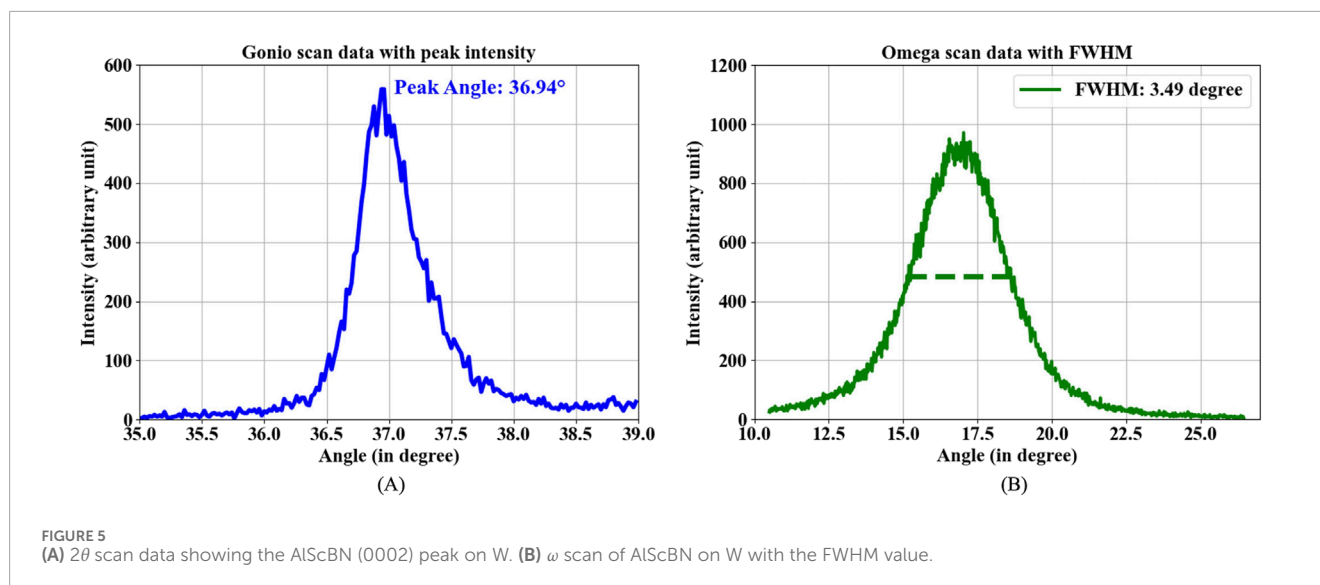


FIGURE 4 XRD ω scan data showing the full width half maximum (FWHM) variation with (A) target-to-substrate distance, (B) N₂ flow rate, and (C) temperature.



3.3 Film surface quality

The presence of abnormally oriented grains (AOGs) was observed using SEM in order to assess the surface quality of the films deposited on Si (100) substrates. According to reports, the density of the AOGs increases as the Sc content in the film increases (Fichtner et al., 2017; Assylbekova, 2022). The elevated concentration of AOGs in the film increases the film's roughness, degrades the film quality, and reduces the piezoelectric response as well as the quality factor in piezoelectric acoustic resonators (Sandu et al., 2019; Liu et al., 2020). Figure 6 depicts the surface quality of thin films under different process conditions: Figure 6A shows the effect of chuck height, Figure 6B depicts the influence of N_2 flow rate, and Figure 6C highlights the impact of deposition temperature. As shown in Figure 6A, increasing the chuck height from 33 mm to 65 mm results in a significant reduction in surface roughness. At lower chuck distances, the surface exhibits many AOGs. Figure 6B shows the effect of the N_2 flow rate on the film texture. A reduction in the N_2 flow rate from 30 to 20 sccm results in a significant decrease in the formation of AOGs, a trend in agreement with prior work in similar deposition systems (Wang et al., 2020; Beaucejour et al., 2022). However, as mentioned earlier, while lower N_2 flow is beneficial to surface smoothness, a flow of 20 sccm outstrips the stability threshold to sustain a plasma in this system. Consequently, a flow rate of 30 sccm was selected as the optimal parameter to ensure sufficient stability for completing the deposition without frequent arcing. Temperature changes during deposition exhibited a moderate influence on surface morphology. From Figure 6C, at 300°C, 350°C and 400°C, the film appears rough with visible AOGs, suggesting reduced uniformity, with the sample at 350°C showing the highest coverage of unwanted grains.

The SEM images were then analyzed using an advanced image recognition technique specifically developed for the quantitative evaluation of abnormally oriented grains (AOGs). This algorithm facilitates the accurate detection and measurement of grains on the substrate with pixel-level precision, enabling precise calculations

of their average area and coverage Spagnuolo et al., 2024. Figure 7 presents the area distribution of the AOGs. A leftward shift in the peak of the curve indicates a higher percentage of smaller-sized AOGs. Narrow and sharp peaks suggest a higher probability of grains being of similar sizes, whereas a broader curve signifies the presence of AOGs with a wide range of different areas. The AOG area distribution curve provides quantitative support for observations made through the visual inspection of SEM images. The leftmost red curve corresponds to Sample 5, which was deposited at a temperature of 300°C, with a N_2 flow rate of 20 sccm and a chuck height of 65 mm. The position of the curve indicates that the surface of this sample contains mostly smaller-sized grains. Furthermore, the narrow peak signifies a high probability of grains with similar sizes or areas, which is desirable. This observation is further supported by the visual inspection of the SEM images for Sample 5. In contrast, samples with broader curves signify the presence of AOGs with a wide range of sizes, indicating greater variability in the grain areas.

Considering the trade-off among the process parameters, an optimal deposition temperature of 300°C, accompanied by a N_2 flow rate of 30 sccm and a distance of 65 mm between the target and substrate, was selected. Under these optimal process conditions, a sample was deposited for the characterization of the piezoelectric and ferroelectric properties of the AlScBN thin film. The roughness of this sample was also measured using AFM. Figure 8 illustrates the surface topography of the AlScBN film deposited on W, with Figure 8A presenting a 2D view of the top surface and Figure 8B providing a 3D perspective of the surface topography. The arithmetic mean roughness (r_a) of the film was measured as 5.518 nm.

3.4 Piezoelectric measurements

The longitudinal piezoelectric coefficient $d_{33,f}$ was assessed using DBLI, resulting in a value of ~ 25 pC/N. It should be noted that while the target composition was precisely controlled, slight

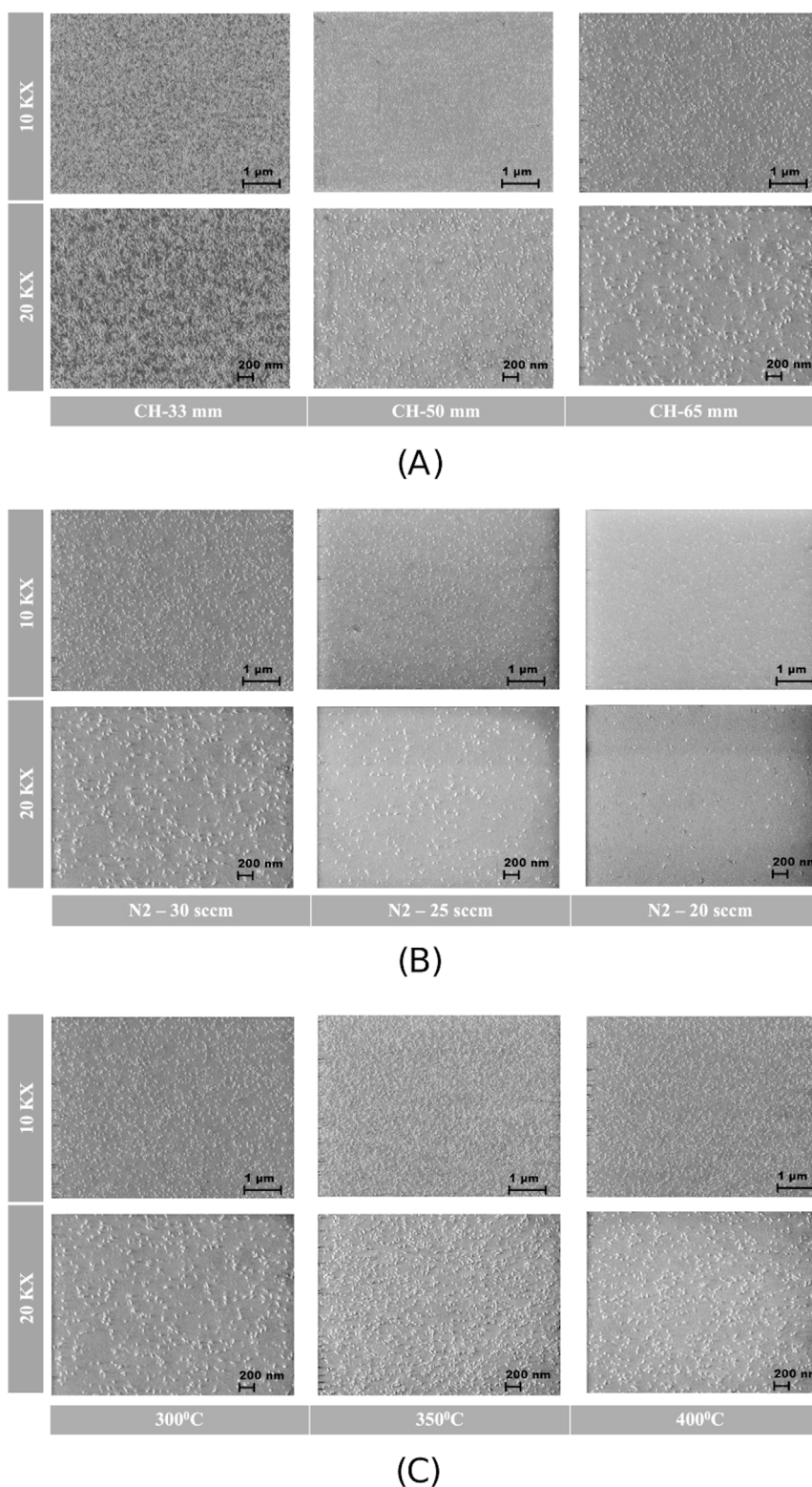


FIGURE 6
SEM visualization of film surface quality for films deposited at different (A) chuck heights, (B) N_2 flow rate, and (C) temperature.

variations might be present in the composition of the deposited film, as available elemental analysis techniques are not reliable for measuring the concentration of light elements such as B.

During this investigation, a 1 kHz AC voltage was applied to the circular top electrode of the test structures to induce piezoelectric displacement, while a common ground connection was established

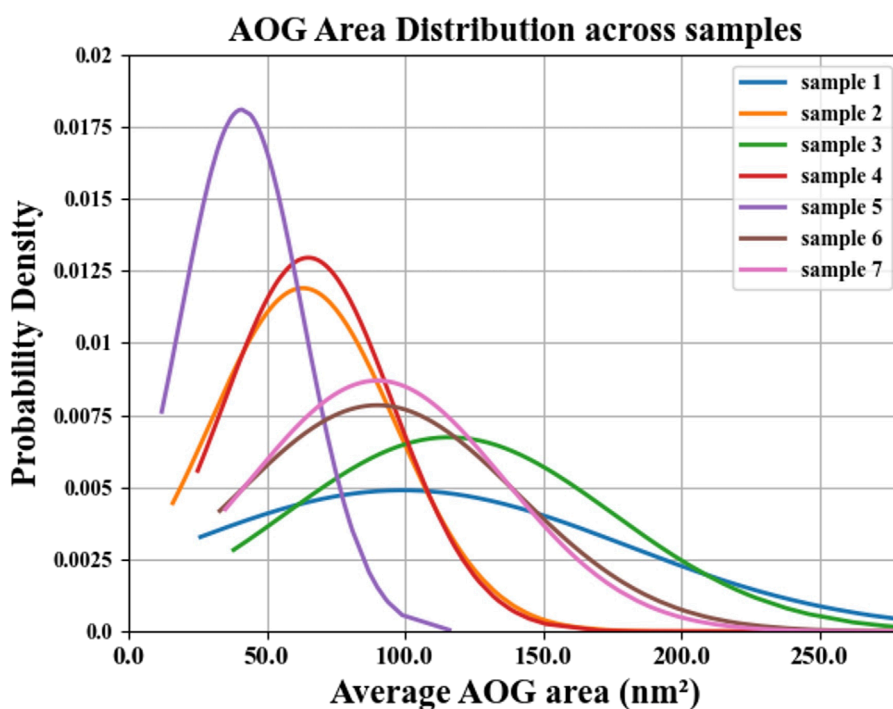


FIGURE 7
AOG area distribution curve for samples deposited on Si.

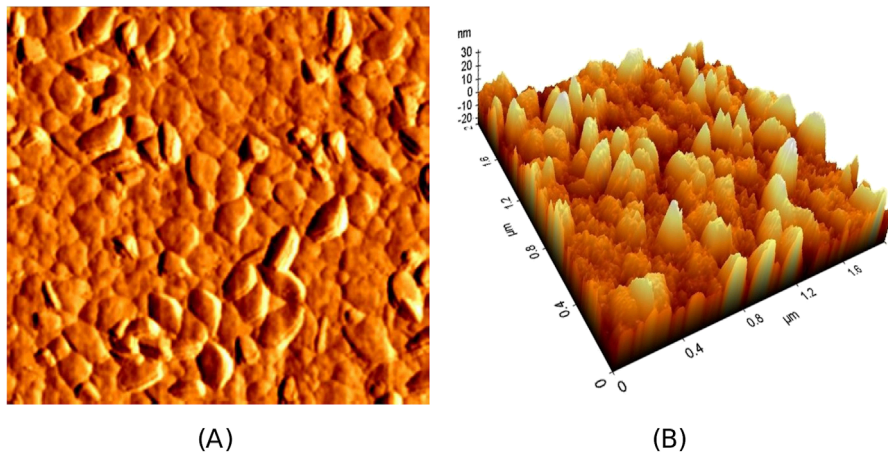
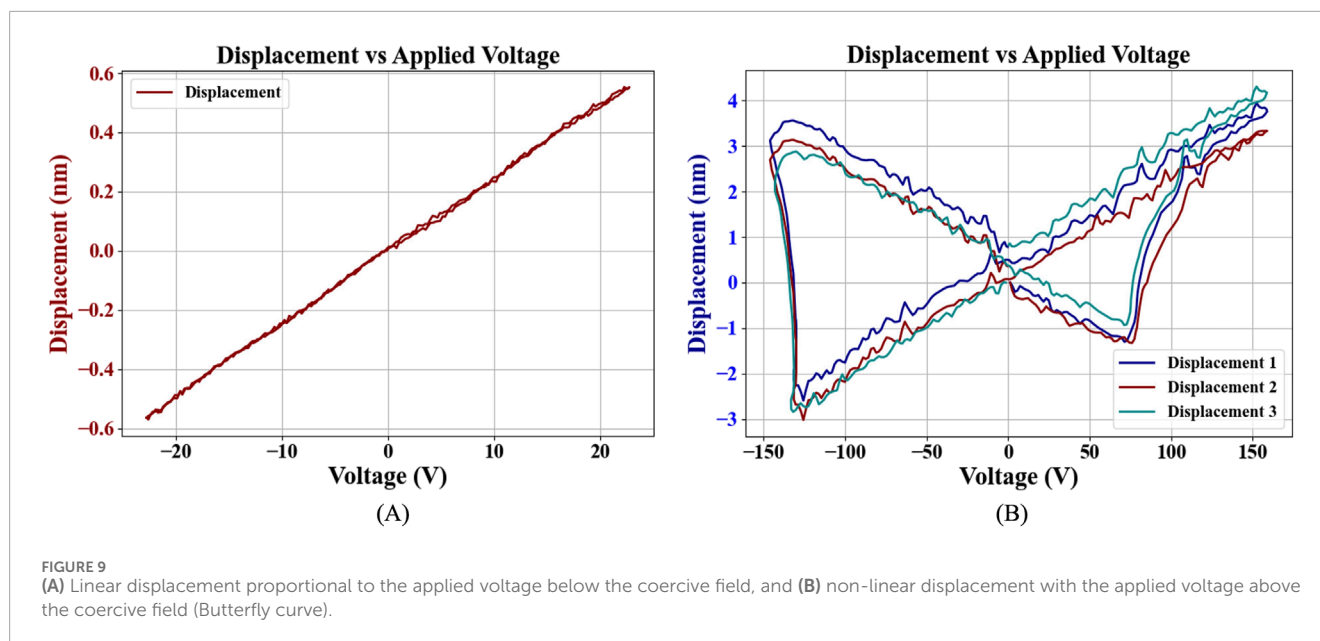


FIGURE 8
Surface imaging by AFM: (A) top-view surface of the AlScBN film deposited on W, and (B) 3D view of the surface.

with the bottom electrode. The measurements were obtained while maintaining the input voltage amplitude below the polarization switching voltage, as illustrated in Figure 9A. Within this range, the displacement exhibited a linear and proportional relationship with the applied voltage, which is characteristic of conventional piezoelectric behavior. Ab-initio estimations from Caro et al. (2015) on Sc-doped AlN and without B co-doping, the d_{33} coefficient at 45% Sc concentration can be as high as 50 pm/V. However, experimental data from Akiyama et al. (2009) on AlScN report values in the 20–30 pC/N range at similar Sc concentrations.

As pointed out by Huang et al. (2006), the estimations done through Berlincourt piezometers might not account for the effects of substrate bending that become prominent in piezoelectric thin films, so even lower d_{33} coefficients might be obtained through interferometric characterization. Regarding estimations of d_{33} in AlN co-doped with Sc and B ions, Jing et al. (2022) presented density functional theory (DFT) calculations for $B_{0.125}Sc_{x-0.125}Al_{1-x}N$ which deliver a d_{33} value of ~ 21 pC/N at $x = 0.5$, corresponding to a Sc concentration of 37.5%. While d_{33} calculations for a Sc concentration of 45% are not reported, the trend delivered from



their model closely matches the value measured in this work. A study from Yuan, Lu et al. (2018a) reports measurement on how AOGs density degrades piezoelectric coupling in AlScN by reducing the d_{33} coefficient. Based on their study, count densities below 100 AOGs per 0.01 m^2 were observed to reduce d_{33} by approximately 10% compared to a well-oriented crystal. In this work, AFM imaging in Figure 8 shows an AOG density well below the affected range reported in Lu et al. (2018a), suggesting that the measured d_{33} coefficient presented in this work is likely close to that of an ideal $\text{Al}_{0.45}\text{Sc}_{0.45}\text{B}_{0.1}\text{N}$ wurtzite crystal. To address the nonlinear voltage-displacement behavior of AlScBN, a butterfly curve is presented in Figure 9B. This curve exemplifies the nonlinear piezoelectric response, depicting the displacement of the material when subjected to an electric field exceeding the coercive field (E_c). The butterfly-shaped displacement-voltage curve is indicative of the ferroelectric nature of the material. This nonlinear and discontinuous response arises due to the reorientation of dipoles under varying electric fields greater than the coercive field (E_c), where the material demonstrates maximum displacement and the majority of domain switching occurs.

3.5 Ferroelectric measurements

Using the same experimental system (DBLI), Dynamic Hysteresis Measurement (DHM) was carried out to showcase the polarization switching, highlighting the remnant polarization ($2P_r = 280 \mu\text{C}/\text{cm}^2$) and coercive field strength, ($E_c^+ = 1.5 \text{ MV}/\text{cm}$, $E_c^- = 2.5 \text{ MV}/\text{cm}$), shown in Figure 10A. This plot exhibits the material's ferroelectric characteristics and demonstrates the reversible switching of polarization in response to an applied electric field. Additionally, Positive Up Negative Down (PUND) measurement was carried out to see the switching current and leakage current visualized in Figure 10B. Both DHM and PUND measurements were carried out by applying more than 150 V to the top electrode of the sample, whereas the bottom

electrode served as the read-out terminal (Pirro et al., 2021). With an increase in voltage, domain walls progressively switch to the direction of the applying field, resulting in the characteristic increase in polarization. Upon reversing the voltage, the domains start to switch in the reverse direction (N polar to M polar or *vice versa*). Nucleation is the initial phase of polarization inversion, where small regions (nuclei) are formed within a ferroelectric material when an external electric field is applied. These nuclei act as starting points for polarization switching (Zhu et al., 2022). As the applied field increases, these domains expand through domain wall motion, which governs the speed and efficiency of the switching process (Gremmel and Fichtner, 2024). The coercive field (E_c) is the minimum electric field required to initiate nucleation. The width of the hysteresis loop indicates the energy loss that occurs during polarization switching, primarily attributed to internal friction, domain wall pinning, and various resistive forces present within the material (Tan et al., 2017). Figure 10A also shows the switching current peaks at the coercive field points from the $I-E$ plot. These peaks correspond to rapid polarization switching events when the electric field overcomes the energy barrier for domain wall movement, which further confirms the ferroelectric characteristics of the material (Tan and Li, 2015). These switching current peaks were also observed in PUND measurements from the $I-V$ plot in the time domain. Figure 10B shows that the peaks arise at the position where the voltage exceeds the polarization switching voltage, plotted as red line. These switching current peaks appear from the displacement current, which is proportional to the rate of change of polarization. When domains switch rapidly, a large current is generated, leading to the observed peaks at the switching voltage points. The coercive field values for AlScBN exhibit asymmetry with $E_c^+ = 1.5 \text{ MV}/\text{cm}$ and $E_c^- = 2.5 \text{ MV}/\text{cm}$ which can be noticed from Figure 10A. This phenomenon might be attributed to the different materials used for the top electrode (Pt) and bottom electrode (W), which influence the polarization switching behavior of the ferroelectric material. The difference in work function between the two electrodes (Pt and W) is essential in

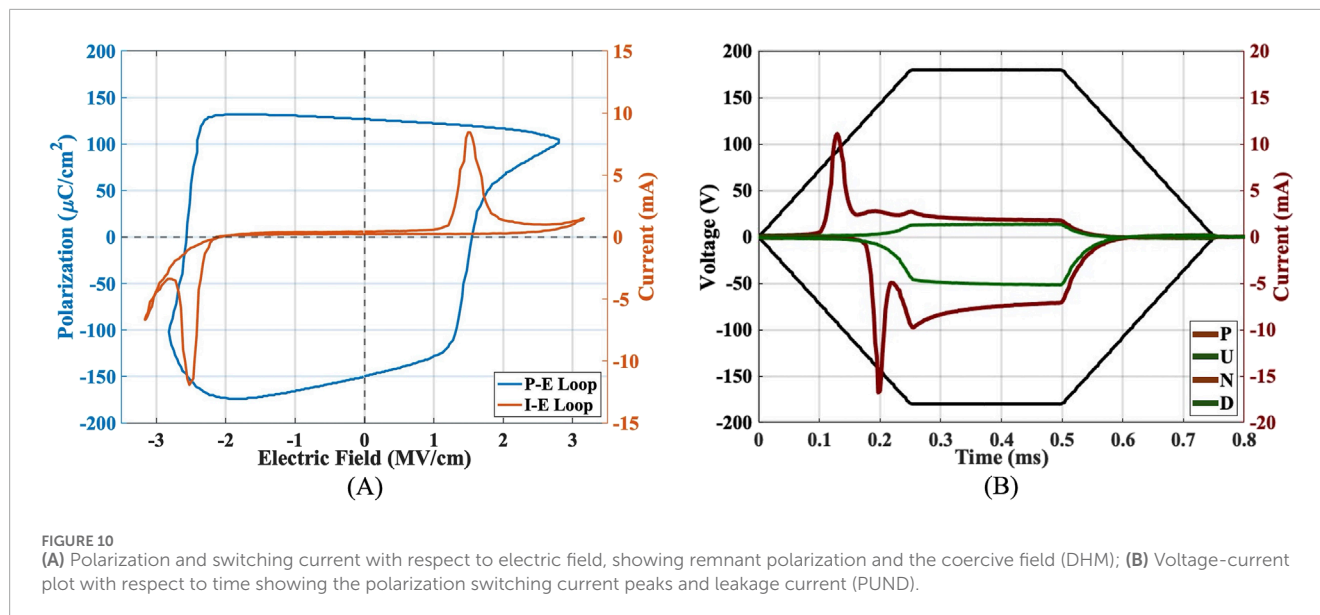


FIGURE 10

(A) Polarization and switching current with respect to electric field, showing remnant polarization and the coercive field (DHM); (B) Voltage-current plot with respect to time showing the polarization switching current peaks and leakage current (PUND).

TABLE 2 Comparison table for piezoelectric (d_{33}) and ferroelectric (P_r and E_c) responses for different materials to state-of-the-art.

Substrate	Target	$d_{33,f}$ max (pm/V)	P_r max ($\mu\text{C}/\text{cm}^2$)	E_c (MV/cm^{-1})	Measuring technique	References
Si/W	$\text{Al}_{0.45}\text{Sc}_{0.45}\text{B}_{0.10}$ (casted)	~25	140	$E_c^+ = 1.5, E_c^- = 2.5$	DBLI	This work
—	$\text{B}_{0.125}\text{Sc}_{x-0.125}\text{Al}_{1-x}$	20.69	94	—	Simulation	Jing et al. (2022)
$\text{Al}_2\text{O}_3/\text{W}$	$\text{Al}_{0.93}\text{B}_{0.07}$	—	136	5.4	Custom built	Hayden et al. (2021)
Si/SiO ₂ /Pt/AlN	$\text{Sc}_x\text{Al}_{1-x}$ [$x = 0.27 - 0.43$]	—	80 - 115	2 - 5	DBLI	Fichtner et al. (2019)
Si/Mo	$\text{Al}_{0.7}\text{Sc}_{0.3}$ alloy	6.79	—	—	DBLI	Liu et al. (2023a)
Si/SiO ₂ /Pt	$\text{Al}_{0.7}\text{Sc}_{0.3}$ alloy	11.8	—	—	DBLI	Mertin et al. (2018)
Si	$\text{Sc}_x\text{Al}_{1-x}$ [$x = 0 - 0.43$]	27.6	—	—	Berlincourt method (Piezotest PM100)	Akiyama et al. (2009)
Al_2O_3	$\text{Sc}_x\text{Al}_{1-x}$ [$x = 0 - 0.41$]	31.6	—	—	Berlincourt method (Piezotest PM300)	Lu et al. (2018b)
Si/Lu	$\text{Al}_{0.53}\text{Sc}_{0.47}$ alloy	35.5	—	—	Berlincourt method (Piezotest PM300)	Hirata et al. (2025)

establishing an asymmetric coercive field (Fields et al., 2023). The work function of platinum (Pt) is about 5.65 eV, whereas tungsten (W) is valued at approximately 4.55 eV (Michaelson, 1977). The variation in work functions leads to the establishment of a built-in electric potential at the interfaces between the ferroelectric and the electrode. The inherent field influences the polarization switching mechanism, requiring distinct external electric fields to achieve polarization switching in each direction (Liu et al., 2001). This built-in field facilitates the transition of polarization toward the W electrode, leading to a reduction in remnant polarization. Additionally, the electrodes exhibit different capabilities in screening

the polarization charge at the thin film interface (Lo and Chen, 2002; Lü and Cao, 2003). This screening reduces the energy barrier for polarization switching toward the Pt electrode, resulting in a lower coercive field (E_c). Nevertheless, Liu et al. reported an asymmetric coercive field in capacitors despite having identical top and bottom electrodes (Al/AlScN/Al) (Liu et al., 2022). This indicates that elements beyond the differences in electrode materials could affect the switching characteristics. The distribution of stress within the film could play a significant role in this asymmetry, which is also applicable to our sample (Yassine et al., 2022). As both remnant polarization and coercive field are higher in the

negative side of the applied electric field direction, we suspect there forms a built-in potential due to residual stress, which made the polarization switching harder in the opposite direction. However, from Figure 10B, the presence of leakage current peaks in both directions, indicated by the dark green lines, is evident. This suggests that the measured remnant polarization ($2P_r$) value may be elevated due to the influence of leakage current. Although the precise impact of leakage current on polarization was not quantified through the PUND measurements presented in Figure 10B, this contribution to the elevated $2P_r$ value of $280 \mu\text{C}/\text{cm}^2$ is certain.

Table 2 showcases a comparative analysis of the piezoelectric and ferroelectric properties of AlScBN, AlBN, and AlScN reported in the literature, along with the respective measuring techniques.

4 Conclusion

The incorporation of Boron (B) into AlScN films was thought to stabilize the wurtzite phase at high Sc concentrations and close to the theoretical instability region of AlScN. A high piezoelectric response was measured, and the ferroelectric hysteresis of AlScBN indicates higher remnant polarization and lower coercive field than 43% doped ScAlN (Fichtner et al., 2020). DBLI measurements showed a longitudinal piezoelectric coefficient ($d_{33,f}$) of $\sim 25 \text{ pC}/\text{N}$. The material exhibited a robust ferroelectric response, featuring a remnant polarization ($2P_r$) of $280 \mu\text{C}/\text{cm}^2$ and coercive fields ranging from $1.5 \text{ MV}/\text{cm}$ (E_c^+) to $2.5 \text{ MV}/\text{cm}$ (E_c^-). However, understanding the ferroelectric response of a relatively thinner AlScBN film is essential for predicting its applicability to different ferroelectric devices. The stress and leakage current contribution in elevated remnant polarization should be studied. The observed asymmetric coercive fields with varying electrode configurations demonstrate the tunability of AlScBN for applications in non-volatile memory, sensors, and actuators (Liu et al., 2016).

Data availability statement

The raw data supporting the conclusions of this article will be made available by the authors upon request.

Author contributions

KS: Conceptualization, Data Curation, Formal Analysis, Investigation, Methodology, Validation, Visualization, Writing–

original draft, Writing–review and editing. PS: Conceptualization, Data curation, Formal Analysis, Investigation, Methodology, Project Administration, Supervision, Validation, Writing–review and editing. LC: Project administration, Software, Supervision, Writing–review and editing. MR: Conceptualization, Funding acquisition, Project Administration, Supervision, Writing–review and editing.

Funding

The author(s) declare that no financial support was received for the research and/or publication of this article.

Acknowledgments

The authors thank the Kostas Nanoscale Technology and Manufacturing Research Center cleanroom facility and its staff for providing the support and required infrastructure for this experimental study.

Conflict of interest

The authors confirm that the research was conducted in the absence of any commercial or financial relationships that could be construed as a potential conflict of interest.

Generative AI statement

The author(s) declare that no Generative AI was used in the creation of this manuscript.

Publisher's note

All claims expressed in this article are solely those of the authors and do not necessarily represent those of their affiliated organizations, or those of the publisher, the editors and the reviewers. Any product that may be evaluated in this article, or claim that may be made by its manufacturer, is not guaranteed or endorsed by the publisher.

References

- Akiyama, M., Kano, K., and Teshigahara, A. (2009). Influence of growth temperature and scandium concentration on piezoelectric response of scandium aluminum nitride alloy thin films. *Appl. Phys. Lett.* 95, 162107. doi:10.1063/1.3251072
- Akiyama, M., Tabaru, T., Nishikubo, K., Teshigahara, A., and Kano, K. (2010). Preparation of scandium aluminum nitride thin films by using scandium aluminum alloy sputtering target and design of experiments. *J. Ceram. Soc. Jpn.* 118, 1166–1169. doi:10.2109/jcersj2.118.1166
- Assylbekova, M. (2022). Aluminum nitride and scandium-doped aluminum nitride materials and devices for beyond 6 GHz communication. Ph.D. thesis. Copyright - Database copyright ProQuest LLC; ProQuest does not claim copyright in the individual underlying works.
- Azarnaminy, A. F., Ou, M., and Mansour, R. R. (2024). Pcm-based reconfigurable acoustic resonators and filters: for potential use in rf front-end applications. *IEEE Microw. Mag.* 25, 48–67. doi:10.1109/MMM.2023.3332286
- Beaucejour, R., Roebisch, V., Kochhar, A., Moe, C. G., Hodge, M. D., and Olsson, R. H. (2022). Controlling residual stress and suppression of anomalous grains in aluminum scandium nitride films grown directly on silicon. *J. Microelectromechanical Syst.* 31, 604–611. doi:10.1109/JMEMS.2022.3167430
- Caro, M. A., Zhang, S., Riekkinen, T., Ylilammi, M., Moram, M. A., Lopez-Acevedo, O., et al. (2015). Piezoelectric coefficients and spontaneous polarization of scAlN. *J. Phys. Condens. Matter* 27, 245901. doi:10.1088/0953-8984/27/24/245901

- Deng, B., Zhang, Y., and Shi, Y. (2024). Examining the ferroelectric characteristics of aluminum nitride-based thin films. *J. Am. Ceram. Soc.* 107, 1571–1581. doi:10.1111/jace.19540
- Fawzy, A., and Zhang, M. (2019). "Piezoelectric thin film materials for acoustic mems devices," in *2019 6th international conference on advanced control circuits and systems (ACCS) 2019 5th international conference on new paradigms in electronics information Technology (PEIT)*, 82–86. doi:10.1109/ACCS-PEIT48329.2019.9062834
- Fichtner, S., Lofink, F., Wagner, B., Schönweger, G., Kreutzer, T.-N., Petraru, A., et al. (2020). "Ferroelectricity in alscn: switching, imprint and sub-150 nm films," in *2020 joint conference of the IEEE international frequency control symposium and international symposium on applications of ferroelectrics (IFCS-isaf)*, 1–4.
- Fichtner, S., Wolff, N., Krishnamurthy, G., Petraru, A., Bohse, S., Lofink, F., et al. (2017). Identifying and overcoming the interface originating c-axis instability in highly Sc enhanced AlN for piezoelectric micro-electromechanical systems. *J. Appl. Phys.* 122, 035301. doi:10.1063/1.4993908
- Fichtner, S., Wolff, N., Lofink, F., Kienle, L., and Wagner, B. (2019). Alscn: a iii-v semiconductor based ferroelectric. *J. Appl. Phys.* 125, 114103. doi:10.1063/1.5084945
- Fields, S. S., Jaszewski, S. T., Lenox, M. K., and Ihlefeld, J. F. (2023). Asymmetric electrode work function customization via top electrode replacement in ferroelectric and field-induced ferroelectric hafnium zirconium oxide thin films. *Adv. Mater. Interfaces* 10, 2202232. doi:10.1002/admi.202202232
- Gremmel, M., and Fichtner, S. (2024). The interplay between imprint, wake-up, and domains in ferroelectric al_{0.70}sc_{0.30}n. *J. Appl. Phys.* 135, 204101. doi:10.1063/5.0197111
- Gund, V., Davaji, B., Lee, H., Casamento, J., Xing, H. G., Jena, D., et al. (2021). "Towards realizing the low-coercive field operation of sputtered ferroelectric Sc_xAl_{1-x}N," in *2021 21st international conference on solid-state sensors, actuators and microsystems (transducers)*, 1064–1067.
- Haider, S. T., Shah, M. A., Lee, D.-G., and Hur, S. (2023). A review of the recent applications of aluminum nitride-based piezoelectric devices. *IEEE Access* 11, 58779–58795. doi:10.1109/ACCESS.2023.3276716
- Hayden, J., Hossain, M. D., Xiong, Y., Ferri, K., Zhu, W., Imperatore, M. V., et al. (2021). Ferroelectricity in boron-substituted aluminum nitride thin films. *Phys. Rev. Mat.* 5, 044412. doi:10.1103/PhysRevMaterials.5.044412
- Hirata, K., Niitsu, K., Anggraini, S. A., Kageura, T., Uehara, M., Yamada, H., et al. (2025). Enhancing the piezoelectric performance of nitride thin films through interfacial engineering. *Mater. Today*. doi:10.1016/j.mattod.2024.12.011
- Huang, Z., Zhang, Q., Corkovic, S., Dorey, R., and Whatmore, R. W. (2006). Comparative measurements of piezoelectric coefficient of pzt films by berlincourt, interferometer, and vibrometer methods. *IEEE Trans. Ultrasonics, Ferroelectr. Freq. Control* 53, 2287–2293. doi:10.1109/TUFFC.2006.175
- Jing, H., Wang, Y., Wen, Q., Cai, X., Liu, K., Li, W., et al. (2022). Large piezoelectric and elastic properties in B and Sc doped wurtzite AlN. *J. Appl. Phys.* 131, 245108. doi:10.1063/5.0090501
- Kurz, N., Ding, A., Urban, D. F., Lu, Y., Kirste, L., Feil, N. M., et al. (2019). Experimental determination of the electro-acoustic properties of thin film alscn using surface acoustic wave resonators. *J. Appl. Phys.* 126, 075106. doi:10.1063/1.5094611
- Liu, C., Chen, B., Li, M., Zhu, Y., and Wang, N. (2020). "Evaluation of the impact of abnormally orientated grains on the performance of scn-based laterally coupled alternating thickness (lcat) mode resonators and lamb wave mode resonators," in *2020 IEEE international ultrasonics symposium (IUS)*, 1–3. doi:10.1109/IUS46767.2020.9251507
- Liu, C., Varghese, B., Liu, P. P., Lin, H., Li, M., and Zhu, Y. (2023a). "Measurement and analysis of longitudinal and transversal effective piezoelectric coefficients 100 nm-500 nm Sc_{0.3}Al_{0.7}N films," in *2023 IEEE international ultrasonics symposium (IUS)*, 1–4. doi:10.1109/IUS51837.2023.10306779
- Liu, F., Fina, I., Bertacco, R., and Fontcuberta, J. (2016). Unravelling and controlling hidden imprint fields in ferroelectric capacitors. *Sci. Rep.* 6, 25028. doi:10.1038/srep25028
- Liu, W., Ko, J., and Zhu, W. (2001). Asymmetric switching behavior of ni/pb1.1(zr0.3ti0.7)o3/pt thin films. *Mater. Lett.* 49, 122–126. doi:10.1016/S0167-577X(00)00354-2
- Liu, X., Ting, J., He, Y., Fiagbenu, M. M. A., Zheng, J., Wang, D., et al. (2022). Reconfigurable compute-in-memory on field-programmable ferroelectric diodes. *Nano Lett.* 22, 7690–7698. doi:10.1021/acs.nanolett.2c03169
- Liu, Z., Wang, X., Ma, X., Yang, Y., and Wu, D. (2023b). Doping effects on the ferroelectric properties of wurtzite nitrides. *Appl. Phys. Lett.* 122, 122901. doi:10.1063/5.0145818
- Lo, V. C., and Chen, Z. J. (2002). Simulation of the effects of space charge and Schottky barriers on ferroelectric thin film capacitor using landau khalatnikov theory. *IEEE Trans. Ultrasonics, Ferroelectr. Freq. Control* 49, 980–986. doi:10.1109/TUFFC.2002.1020168
- Lü, T., and Cao, W. (2003). Influence of imperfect surface on properties of ferroelectric thin film. *Microelectron. Eng.* 66, 818–824. doi:10.1016/S0167-9317(02)01005-5
- Lu, Y., Reusch, M., Kurz, N., Ding, A., Christoph, T., Kirste, L., et al. (2018a). Surface morphology and microstructure of pulsed dc magnetron sputtered piezoelectric aln and alscn thin films. *Phys. status solidi (a)* 215, 1700559. doi:10.1002/pssa.201700559
- Lu, Y., Reusch, M., Kurz, N., Ding, A., Christoph, T., Prescher, M., et al. (2018b). Elastic modulus and coefficient of thermal expansion of piezoelectric Al_{1-x}Sc_xN (up to x = 0.41) thin films. *Appl. Mater.* 6, 076105. doi:10.1063/1.5040190
- Manna, S., Talley, K. R., Gorai, P., Mangum, J. S., Zakutayev, A., Brennecke, G. L., et al. (2018). Enhanced piezoelectric response of aln via crn alloying. *Phys. Rev. Appl.* 9, 034026. doi:10.1103/physrevapplied.9.034026
- Matloub, R., Hadad, M., Mazzalai, A., Chidambaram, N., Moulard, G., Sandu, C. S., et al. (2013). Piezoelectric Al_{1-x}Sc_xN thin films: a semiconductor compatible solution for mechanical energy harvesting and sensors. *Appl. Phys. Lett.* 102. doi:10.1063/1.4800231
- Mertin, S., Heinz, B., Mazzalar, A., Schmitz-Kempen, T., Tiedke, S., and Pensala, T. (2018). High-volume production and non-destructive piezo-property mapping of 33In. *2018 IEEE International Ultrasonics Symposium (IUS)*. 1–4. doi:10.1109/ULTSYM.2018.8580120
- Michaelson, H. B. (1977). The work function of the elements and its periodicity. *J. Appl. Phys.* 48, 4729–4733. doi:10.1063/1.323539
- Murali, P. (2008). Recent progress in materials issues for piezoelectric MEMS. *J. Am. Ceram. Soc.* 91, 1385–1396. doi:10.1111/j.1551-2916.2008.02421.x
- Murali, P., Polcawich, R. G., and Troler-McKinstry, S. (2009). Piezoelectric thin films for sensors, actuators, and energy harvesting. *MRS Bull.* 34, 658–664. doi:10.1557/mrs2009.177
- Olsson, R. H., Tang, Z., and D'Agati, M. (2020). "Doping of aluminum nitride and the impact on thin film piezoelectric and ferroelectric device performance," in *2020 IEEE custom integrated circuits conference (CICC)*, 1–6.
- Pirro, M., Herrera, B., Assylbekova, M., Giribaldi, G., Colombo, L., and Rinaldi, M. (2021). "Characterization of dielectric and piezoelectric properties of ferroelectric alscn thin films," in *2021 IEEE 34th international conference on micro electro mechanical systems (MEMS)*, 646–649. doi:10.1109/MEMS51782.2021.9375427
- Pirro, M., Zhao, X., Herrera, B., Simeoni, P., and Rinaldi, M. (2022). Effect of substrate-rf on sub-200 nm al_{0.7}sc_{0.3}n thin films. *Micromachines* 13, 877. doi:10.3390/mi13060877
- Saha, K. (2023). *Characterization of scandium-doped aluminum nitride thin films for bulk acoustic wave resonators*. Politecnico di Torino: Ph.D. thesis.
- Sandu, C. S., Parsapour, F., Mertin, S., Pashchenko, V., Matloub, R., LaGrange, T., et al. (2019). Abnormal grain growth in AlScN thin films induced by complexion formation at crystallite interfaces. *Phys. status solidi (a)* 216, 1800569. doi:10.1002/pssa.201800569
- Sivaramakrishnan, S., Mardilovich, P., Mason, A., Roelofs, A., Schmitz-Kempen, T., and Tiedke, S. (2013). Electrode size dependence of piezoelectric response of lead zirconate titanate thin films measured by double beam laser interferometry. *Appl. Phys. Lett.* 103, 132904. doi:10.1063/1.4821948
- Sivaramakrishnan, S., Mardilovich, P., Schmitz-Kempen, T., and Tiedke, S. (2018). Concurrent wafer-level measurement of longitudinal and transverse effective piezoelectric coefficients (d_{33} , f and e_{31} , f) by double beam laser interferometry. *J. Appl. Phys.* 123, 014103. doi:10.1063/1.5019568
- Spagnuolo, L., Colombo, L., Gubinelli, W., Saha, K., Simeoni, P., and Rinaldi, M. (2024). "An image recognition technique for the quantitative analysis of abnormally oriented grains in advanced piezoelectric material," in *2024 IEEE ultrasonics, ferroelectrics, and frequency control joint symposium (UFFC-fs)*, 1–3. doi:10.1109/UFFC-JS60046.2024.10794029
- Startt, J., Quazi, M., Sharma, P., Vazquez, I., Poudyal, A., Jackson, N., et al. (2023). Unlocking AlN piezoelectric performance with earth-abundant dopants. *Adv. Electron. Mater.* 9, 2201187. doi:10.1002/aeml.202201187
- Stoney, G. G. (1909). The tension of metallic films deposited by electrolysis. *Proc. R. Soc. Lond. Ser. A. Contain. Pap. a Math. Phys. Character* 82, 172–175.
- Tabrizian, R., Rais-Zadeh, M., and Ayazi, F. (2009). "Effect of phonon interactions on limiting the f.q product of micromechanical resonators," in *Transducers 2009 - 2009 international solid-state sensors, actuators and microsystems conference*, 2131–2134. doi:10.1109/SENSOR.2009.5285627
- Tan, G., and Li, W. (2015). Ferroelectricity and ferromagnetism of m-type lead hexaferrite. *J. Am. Ceram. Soc.* 98, 1812–1817. doi:10.1111/jace.13530
- Tan, X., Xu, Z., Liu, X., and Fan, Z. H. (2017). Double hysteresis loops at room temperature in nanbo3-based lead-free antiferroelectric ceramics. *Mater. Res. Lett.* 6, 159–164. doi:10.1080/21663831.2017.1419994
- Tasnádi, F., Alling, B., Höglund, C., Wingqvist, G., Birch, J., Hultman, L., et al. (2010). Origin of the anomalous piezoelectric response in wurtzite sc_xal_{1-x}N alloys. *Phys. Rev. Lett.* 104, 137601. doi:10.1103/PhysRevLett.104.137601
- Tholander, C., Tasnádi, F., Abrikosov, I. A., Hultman, L., Birch, J., and Alling, B. (2015). Large piezoelectric response of quaternary wurtzite nitride alloys and its physical origin from first principles. *Phys. Rev. B* 92, 174119. doi:10.1103/PhysRevB.92.174119
- Wang, D., Zheng, J., Tang, Z., D'Agati, M., Gharavi, P. S. M., Liu, X., et al. (2020). "Ferroelectric c-axis textured aluminum scandium nitride thin films of

100 nm thickness,” in *2020 joint conference of the IEEE international frequency control symposium and international symposium on applications of ferroelectrics (IFCS-isaf)*, 1–4.

Wingqvist, G., Tasnádi, F., Žukauskaitė, A., Birch, J., Arwin, H., and Hultman, L. (2010). Increased electromechanical coupling in w-ScxAl1-xN. *Appl. Phys. Lett.* 97. doi:10.1063/1.3489939

Xue, Y., Liu, Y., Zhou, C., and Zhang, X. Y. (2024). Acoustic wave devices based on piezoelectric/ferroelectric thin films for high-frequency communication systems and sensing applications. *Ceram. Int.* 50, 52051–52058. doi:10.1016/j.ceramint.2024.03.212

Yassine, M., Nair, A., Fammels, J., Wade, E., Fu, Z., Yassine, A., et al. (2022). Influence of structural properties on the ferroelectric behavior of hexagonal alscn. *J. Appl. Phys.* 132, 114101. doi:10.1063/5.0103578

Zhu, W., Hayden, J., He, F., Yang, J., Tipsawat, P., Hossain, M. D., et al. (2021). Strongly temperature dependent ferroelectric switching in aln, al1-xscxn, and al1-xbxn thin films. *Appl. Phys. Lett.* 119. doi:10.1063/5.0057869

Zhu, W., He, F., Hayden, J., Fan, Z., Yang, J. I., Maria, J.-P., et al. (2022). Wake-up in Al_{1-x}B_xN ferroelectric films. *Adv. Electron. Mater.* 8, 2100931. doi:10.1002/aelm.202100931